Investigation of artifacts in retinal and choroidal OCT angiography with a contrast agent

MARCEL T. BERNUCCI,[1] CONRAD W. MERKLE,[1] AND VIVEK J. SRINIVASAN[1,2,*]

[1]Department of Biomedical Engineering, University of California Davis, Davis, California, USA
[2]Department of Ophthalmology and Vision Science, University of California Davis School of Medicine, Sacramento, California, USA
*vjsriniv@ucdavis.edu

Abstract: Optical coherence tomography angiography (OCTA) has recently emerged for imaging vasculature in clinical ophthalmology. Yet, OCTA images contain artifacts that remain challenging to interpret. To help explain these artifacts, we perform contrast-enhanced OCTA with a custom-designed wide-field ophthalmoscope in rats *in vivo*. We choose an intravascular contrast agent (Intralipid) with particles that are more isotropically scattering and more symmetrically shaped than red blood cells (RBCs). Then, by examining how OCTA artifacts change after contrast agent injection, we attribute OCTA artifacts to RBC-specific properties. In this work, we investigate retinal and choroidal OCTA in rats with or without melanosomes, both before and after contrast agent injection, at a wavelength at which scattering dominates the image contrast (1300 nm). First, baseline images suggest that high backscattering of choroidal melanosomes accounts for the relatively dark appearance of choroidal vessel lumens in OCTA. Second, Intralipid injection tends to eliminate the hourglass pattern artifact in OCTA images of vessel lumens and highlights vertical capillaries that were previously faint in OCTA, showing that RBC orientation is important in determining OCTA signal. Third, Intralipid injection increases lumen signal without significantly affecting the tails, suggesting that projection artifacts, or tails, are due to RBC multiple scattering. Fourth, Intralipid injection increases the side-to-top signal ratio less in choroidal vessel lumens of pigmented rats, suggesting that melanosome multiple scattering makes the hourglass artifact less prominent. This study provides the first direct experimental *in vivo* evidence to explain light scattering-related artifacts in OCTA.

References and links

1. W. Choi, K. J. Mohler, B. Potsaid, C. D. Lu, J. J. Liu, V. Jayaraman, A. E. Cable, J. S. Duker, R. Huber, and J. G. Fujimoto, "Choriocapillaris and choroidal microvasculature imaging with ultrahigh speed OCT angiography," PLoS One **8**(12), e81499 (2013).
2. D. Y. Kim, J. Fingler, R. J. Zawadzki, S. S. Park, L. S. Morse, D. M. Schwartz, S. E. Fraser, and J. S. Werner, "Optical imaging of the chorioretinal vasculature in the living human eye," Proc. Natl. Acad. Sci. U.S.A. **110**(35), 14354–14359 (2013).
3. Y. Jia, S. T. Bailey, D. J. Wilson, O. Tan, M. L. Klein, C. J. Flaxel, B. Potsaid, J. J. Liu, C. D. Lu, M. F. Kraus, J. G. Fujimoto, and D. Huang, "Quantitative optical coherence tomography angiography of choroidal neovascularization in age-related macular degeneration," Ophthalmology **121**(7), 1435–1444 (2014).
4. Y. Jia, E. Wei, X. Wang, X. Zhang, J. C. Morrison, M. Parikh, L. H. Lombardi, D. M. Gattey, R. L. Armour, B. Edmunds, M. F. Kraus, J. G. Fujimoto, and D. Huang, "Optical coherence tomography angiography of optic disc perfusion in glaucoma," Ophthalmology **121**(7), 1322–1332 (2014).
5. Y. Jia, S. T. Bailey, T. S. Hwang, S. M. McClintic, S. S. Gao, M. E. Pennesi, C. J. Flaxel, A. K. Lauer, D. J. Wilson, J. Hornegger, J. G. Fujimoto, and D. Huang, "Quantitative optical coherence tomography angiography of vascular abnormalities in the living human eye," Proc. Natl. Acad. Sci. U.S.A. **112**(18), E2395–E2402 (2015).

6.   A. Ishibazawa, T. Nagaoka, A. Takahashi, T. Omae, T. Tani, K. Sogawa, H. Yokota, and A. Yoshida, "Optical Coherence Tomography Angiography in Diabetic Retinopathy: A Prospective Pilot Study," Am. J. Ophthalmol. **160**(1), 35–44 (2015).

7.   R. F. Spaide, "Optical Coherence Tomography Angiography Signs of Vascular Abnormalization With Antiangiogenic Therapy for Choroidal Neovascularization," Am. J. Ophthalmol. **160**(1), 6–16 (2015).

8.   T. E. de Carlo, M. A. Bonini Filho, A. T. Chin, M. Adhi, D. Ferrara, C. R. Baumal, A. J. Witkin, E. Reichel, J. S. Duker, and N. K. Waheed, "Spectral-domain optical coherence tomography angiography of choroidal neovascularization," Ophthalmology **122**(6), 1228–1238 (2015).

9.   P. Cimalla, J. Walther, M. Mittasch, and E. Koch, "Shear flow-induced optical inhomogeneity of blood assessed in vivo and in vitro by spectral domain optical coherence tomography in the 1.3 μm wavelength range," J. Biomed. Opt. **16**(11), 116020 (2011).

10. Y. Muraoka, A. Tsujikawa, T. Murakami, K. Ogino, K. Kumagai, K. Miyamoto, A. Uji, and N. Yoshimura, "Morphologic and functional changes in retinal vessels associated with branch retinal vein occlusion," Ophthalmology **120**(1), 91–99 (2013).

11. C. W. Merkle, C. Leahy, and V. J. Srinivasan, "Dynamic contrast optical coherence tomography images transit time and quantifies microvascular plasma volume and flow in the retina and choriocapillaris," Biomed. Opt. Express **7**(10), 4289–4312 (2016).

12. A. Willerslev, X. Q. Li, I. C. Munch, and M. Larsen, "Flow patterns on spectral-domain optical coherence tomography reveal flow directions at retinal vessel bifurcations," Acta Ophthalmol. **92**(5), 461–464 (2014).

13. A. Zhang, Q. Zhang, and R. K. Wang, "Minimizing projection artifacts for accurate presentation of choroidal neovascularization in OCT micro-angiography," Biomed. Opt. Express **6**(10), 4130–4143 (2015).

14. M. Zhang, T. S. Hwang, J. P. Campbell, S. T. Bailey, D. J. Wilson, D. Huang, and Y. Jia, "Projection-resolved optical coherence tomographic angiography," Biomed. Opt. Express **7**(3), 816–828 (2016).

15. R. F. Spaide, J. G. Fujimoto, and N. K. Waheed, "Image Artifacts in Optical Coherence Angiography," Retina **35**(11), 2163–2180 (2015).

16. R. Hua and H. Wang, "Dark Signals in the Choroidal Vasculature on Optical Coherence Tomography Angiography: An Artefact or Not?" J. Ophthalmol. **2017**, 5498125 (2017).

17. H. C. Hendargo, R. P. McNabb, A.-H. Dhalla, N. Shepherd, and J. A. Izatt, "Doppler velocity detection limitations in spectrometer-based versus swept-source optical coherence tomography," Biomed. Opt. Express **2**(8), 2175–2188 (2011).

18. A. Willerslev, X. Q. Li, P. Cordtz, I. C. Munch, and M. Larsen, "Retinal and choroidal intravascular spectral-domain optical coherence tomography," Acta Ophthalmol. **92**(2), 126–132 (2014).

19. S. H. Yun, G. Tearney, J. de Boer, and B. Bouma, "Motion artifacts in optical coherence tomography with frequency-domain ranging," Opt. Express **12**(13), 2977–2998 (2004).

20. T. L. Swaantje Petersa, D. Kokkinoua, K. U. Bartz-Schmidta, and U. Schraermeyera, "Melanin Protects Choroidal Blood Vessels against Light Toxicity," Verlag der Zeitschrift für Naturforschung, (February 24, 2006).

21. V. Gupta, A. Gupta, and M. R. Dogra, *ATLAS Optical Coherence Tomography of Macular Diseases and Glaucoma* (Jaypee Brothers Publishers).

22. C. V. Regatieri, L. Branchini, J. G. Fujimoto, and J. S. Duker, "Choroidal imaging using spectral-domain Optical Coherence Tomography," Retina **32**(5), 865–876 (2012).

23. K. V. Bhavsar, L. Branchini, H. Shah, C. V. Regatieri, and J. S. Duker, "Choroidal Thickness in Retinal Pigment Epithelial Tear as Measured by Spectral Domain Optical Coherence Tomography," Retina **34**(1), 63–68 (2014).

24. E. Götzinger, M. Pircher, W. Geitzenauer, C. Ahlers, B. Baumann, S. Michels, U. Schmidt-Erfurth, and C. K. Hitzenberger, "Retinal pigment epithelium segmentation by polarization sensitive optical coherence tomography," Opt. Express **16**(21), 16410–16422 (2008).

25. B. Baumann, S. O. Baumann, T. Konegger, M. Pircher, E. Götzinger, F. Schlanitz, C. Schütze, H. Sattmann, M. Litschauer, U. Schmidt-Erfurth, and C. K. Hitzenberger, "Polarization sensitive optical coherence tomography of melanin provides intrinsic contrast based on depolarization," Biomed. Opt. Express **3**(7), 1670–1683 (2012).

26. B. Baumann, J. Schirmer, S. Rauscher, S. Fialová, M. Glösmann, M. Augustin, M. Pircher, M. Gröger, and C. K. Hitzenberger, "Melanin Pigmentation in Rat Eyes: In Vivo Imaging by Polarization-Sensitive Optical Coherence Tomography and Comparison to Histology," Invest. Ophthalmol. Vis. Sci. **56**(12), 7462–7472 (2015).

27. S. S. Sandhu and S. J. Talks, "Correlation of optical coherence tomography, with or without additional colour fundus photography, with stereo fundus fluorescein angiography in diagnosing choroidal neovascular membranes," Br. J. Ophthalmol. **89**(8), 967–970 (2005).

28. R. A. C. van Huet, N. M. Bax, S. C. Westeneng-Van Haaften, M. Muhamad, M. N. Zonneveld-Vrieling, L. H. Hoefsloot, F. P. M. Cremers, C. J. F. Boon, B. J. Klevering, and C. B. Hoyng, "Foveal Sparing in Stargardt Disease," Invest. Ophthalmol. Vis. Sci. **55**(11), 7467–7478 (2014).

29. M. Salas, M. Augustin, L. Ginner, A. Kumar, B. Baumann, R. Leitgeb, W. Drexler, S. Prager, J. Hafner, U. Schmidt-Erfurth, and M. Pircher, "Visualization of micro-capillaries using optical coherence tomography angiography with and without adaptive optics," Biomed. Opt. Express **8**(1), 207–222 (2017).

30. K. Kurokawa, K. Sasaki, S. Makita, Y.-J. Hong, and Y. Yasuno, "Three-dimensional retinal and choroidal capillary imaging by power Doppler optical coherence angiography with adaptive optics," Opt. Express **20**(20), 22796–22812 (2012).

31. C. Leahy, H. Radhakrishnan, M. Bernucci, and V. J. Srinivasan, "Imaging and graphing of cortical vasculature using dynamically focused optical coherence microscopy angiography," J. Biomed. Opt. **21**(2), 020502 (2016).
32. M. Hammer, A. N. Yaroslavsky, and D. Schweitzer, "A scattering phase function for blood with physiological haematocrit," Phys. Med. Biol. **46**(3), N65–N69 (2001).
33. P. E. Z. Tan, C. Balaratnasingam, J. Xu, Z. Mammo, S. X. Han, P. Mackenzie, A. W. Kirker, D. Albiani, A. B. Merkur, M. V. Sarunic, and D.-Y. Yu, "Quantitative Comparison of Retinal Capillary Images Derived By Speckle Variance Optical Coherence Tomography With Histology," Invest. Ophthalmol. Vis. Sci. **56**(6), 3989–3996 (2015).
34. S. Jacques, "Optical Absorption of Melanin," Oregon Medical Laser Center. *http://omlc.ogi.edu/spectra/melanin/mua.html*.
35. Y. Pan, J. You, N. D. Volkow, K. Park, and C. Du, "Ultrasensitive detection of 3D cerebral microvascular network dynamics in vivo," Neuroimage **103**, 492–501 (2014).
36. C. W. Merkle and V. J. Srinivasan, "Laminar microvascular transit time distribution in the mouse somatosensory cortex revealed by Dynamic Contrast Optical Coherence Tomography," Neuroimage **125**, 350–362 (2016).
37. L. G. Henyey and J. L. Greenstein, "Diffuse radiation in the galaxy," Astrophys. J. **93**, 70–83 (1941).
38. A. N. Yaroslavsky, I. V. Yaroslavsky, T. Goldbach, and H.-J. Schwarzmaier, "Optical properties of blood in the near-infrared spectral range," in Optical Diagnostics of Living Cells and Biofluids (1996), 314–324.
39. A. Roggan, M. Friebel, K. Dö Rschel, A. Hahn, and G. Mü Ller, "Optical Properties of Circulating Human Blood in the Wavelength Range 400-2500 nm," J. Biomed. Opt. **4**(1), 36–46 (1999).
40. V. M. Kodach, D. J. Faber, J. van Marle, T. G. van Leeuwen, and J. Kalkman, "Determination of the scattering anisotropy with optical coherence tomography," Opt. Express **19**(7), 6131–6140 (2011).
41. P. B. Canham, R. F. Potter, and D. Woo, "Geometric accommodation between the dimensions of erythrocytes and the calibre of heart and muscle capillaries in the rat," J. Physiol. **347**(1), 697–712 (1984).
42. C. M. Hawkey, P. M. Bennett, S. C. Gascoyne, M. G. Hart, and J. K. Kirkwood, "Erythrocyte size, number and haemoglobin content in vertebrates," Br. J. Haematol. **77**(3), 392–397 (1991).
43. P. Bartsch, W. Ball, W. Rosenzweig, and S. Salman, "Size of red blood corpuscles and their nucleus in fifty North American birds," Auk **54**(4), 516–519 (1937).
44. S. Banerjee, K. Misra, S. Banerjee, and S. Ray-Chaudhuri, "Chromosome numbers, genome sizes, cell volumes and evolution of snake-head fish (family Channidae)," J. Fish Biol. **33**(5), 781–789 (1988).
45. W. Frair, "Sea turtle red blood cell parameters correlated with carapace lengths," Comp. Biochem. Physiol. Part A. Physiol. **56**(4), 467–472 (1977).
46. T. R. Gregory, "The bigger the C-value, the larger the cell: genome size and red blood cell size in vertebrates," Blood Cells Mol. Dis. **27**(5), 830–843 (2001).
47. M. Diez-Silva, M. Dao, J. Han, C.-T. Lim, and S. Suresh, "Shape and Biomechanical Characteristics of Human Red Blood Cells in Health and Disease," MRS Bull. **35**(5), 382–388 (2010).
48. C. M. Dickson, C. T. Ogbuah, and T. G. Smith, "The role of gamont entry into erythrocytes in the specificity of Hepatozoon species (Apicomplexa: Adeleida) for their frog hosts," J. Parasitol. **99**(6), 1028–1033 (2013).
49. W. Frair, "Turtle red blood cell packed volumes, sizes, and numbers," Herpetologica **33**, 167–190 (1977).
50. L. Goniakow, "Respiration, resistance to hypotonic solutions and ultrastructure of erythrocytes of Salamandra-salamandra," Bulletin de l'Academie Polonaise des Sciences-Serie des Sciences Biologiques 22, 59 (1974).
51. G. Gulliver, *Observations on the Sizes and Shapes of the Red Corpuscles of the Blood of Vertebrates* (1875).
52. D. P. Popescu and M. G. Sowa, "In Vitro Assessment of Optical Properties of Blood by Applying the Extended Huygens-Fresnel Principle to Time-Domain Optical Coherence Tomography Signal at 1300 nm," Int. J. Biomed. Imaging **2008**, 591618 (2008).
53. N. Bosschaart, G. J. Edelman, M. C. G. Aalders, T. G. van Leeuwen, and D. J. Faber, "A literature review and novel theoretical approach on the optical properties of whole blood," Lasers Med. Sci. **29**(2), 453–479 (2014).
54. H. Noguchi and G. Gompper, "Shape transitions of fluid vesicles and red blood cells in capillary flows," Proc. Natl. Acad. Sci. U.S.A. **102**(40), 14159–14164 (2005).
55. D. A. Fedosov, M. Peltomäki, and G. Gompper, "Deformation and dynamics of red blood cells in flow through cylindrical microchannels," Soft Matter **10**(24), 4258–4267 (2014).
56. C. Duprat and H. A. Shore, *Fluid-Structure Interactions in Low-Reynolds-Number Flows* (Royal Society of Chemistry, 2015).
57. V. J. Srinivasan, T. H. Ko, M. Wojtkowski, M. Carvalho, A. Clermont, S.-E. Bursell, Q. H. Song, J. Lem, J. S. Duker, J. S. Schuman, and J. G. Fujimoto, "Noninvasive Volumetric Imaging and Morphometry of the Rodent Retina with High-Speed, Ultrahigh-Resolution Optical Coherence Tomography," Invest. Ophthalmol. Vis. Sci. **47**(12), 5522–5528 (2006).
58. B. Baumann, W. Choi, B. Potsaid, D. Huang, J. S. Duker, and J. G. Fujimoto, "Swept source/Fourier domain polarization sensitive optical coherence tomography with a passive polarization delay unit," Opt. Express **20**(9), 10229–10241 (2012).
59. J. Yi, W. Liu, S. Chen, V. Backman, N. Sheibani, C. M. Sorenson, A. A. Fawzi, R. A. Linsenmeier, and H. F. Zhang, "Visible light optical coherence tomography measures retinal oxygen metabolic response to systemic oxygenation," Light Sci. Appl. **4**(9), e334 (2015).
60. J. Liu, I. Grulkowski, M. Kraus, B. Potsaid, C. D Lu, B. Baumann, J. Duker, J. Hornegger, and J. G Fujimoto, "In vivo imaging of the rodent eye with swept source/Fourier domain OCT," Biomed. Opt. Express **4**, 351–363 (2013).

61. W. Song, Q. Wei, W. Liu, T. Liu, J. Yi, N. Sheibani, A. A. Fawzi, R. A. Linsenmeier, S. Jiao, and H. F. Zhang, "A combined method to quantify the retinal metabolic rate of oxygen using photoacoustic ophthalmoscopy and optical coherence tomography," Sci. Rep. **4**, 6525 (2014).
62. S. Jiao, M. Jiang, J. Hu, A. Fawzi, Q. Zhou, K. K. Shung, C. A. Puliafito, and H. F. Zhang, "Photoacoustic ophthalmoscopy for in vivo retinal imaging," Opt. Express **18**(4), 3967–3972 (2010).
63. X. Zhang, J. Hu, R. W Knighton, X.-R. Huang, C. A Puliafito, and S. Jiao, "Visible light optical coherence tomography for in vivo imaging the spectral contrasts of the retinal nerve fiber layer," Proc. SPIE **19**, 19653–19659 (2011).
64. N. Zabouri, J. F. Bouchard, and C. Casanova, "Cannabinoid receptor type 1 expression during postnatal development of the rat retina," J. Comp. Neurol. **519**(7), 1258–1280 (2011).
65. D. C. Lozano and M. D. Twa, "Quantitative Evaluation of Factors Influencing the Repeatability of SD-OCT Thickness Measurements in the Rat," Invest. Ophthalmol. Vis. Sci. **53**(13), 8378–8385 (2012).
66. E. Orhan, D. Dalkara, M. Neuillé, C. Lechauve, C. Michiels, S. Picaud, T. Léveillard, J.-A. Sahel, M. I. Naash, M. M. Lavail, C. Zeitz, and I. Audo, "Genotypic and Phenotypic Characterization of P23H line 1 Rat Model," PLoS One **10**(5), e0127319 (2015).
67. Z. Nafar, M. Jiang, R. Wen, and S. Jiao, "Visible-light optical coherence tomography-based multimodal retinal imaging for improvement of fluorescent intensity quantification," Biomed. Opt. Express **7**(9), 3220–3229 (2016).
68. L. C. Ho, B. Wang, I. P. Conner, Y. van der Merwe, R. A. Bilonick, S.-G. Kim, E. X. Wu, I. A. Sigal, G. Wollstein, J. S. Schuman, and K. C. Chan, "In Vivo Evaluation of White Matter Integrity and Anterograde Transport in Visual System After Excitotoxic Retinal Injury With Multimodal MRI and OCT," Invest. Ophthalmol. Vis. Sci. **56**(6), 3788–3800 (2015).
69. P. Vasa, J. A. Dharmadhikari, A. K. Dharmadhikari, R. Sharma, M. Singh, and D. Mathur, "Supercontinuum generation in water by intense, femtosecond laser pulses under anomalous chromatic dispersion," Phys. Rev. A **89**(4), 043834 (2014).
70. Z. Zhi, W. Cepurna, E. Johnson, T. Shen, J. Morrison, and R. K. Wang, "Volumetric and quantitative imaging of retinal blood flow in rats with optical microangiography," Biomed. Opt. Express **2**(3), 579–591 (2011).
71. R. Nachabé, B. H. Hendriks, A. E. Desjardins, M. van der Voort, M. B. van der Mark, and H. J. Sterenborg, "Estimation of lipid and water concentrations in scattering media with diffuse optical spectroscopy from 900 to 1,600 nm," J. Biomed. Opt. **15**(3), 037015 (2010).
72. S. Kedenburg, M. Vieweg, T. Gissibl, and H. Giessen, "Linear refractive index and absorption measurements of nonlinear optical liquids in the visible and near-infrared spectral region," Opt. Mater. Express **2**(11), 1588–1611 (2012).
73. A. Hughes and H. Wässle, "An estimate of image quality in the rat eye," Invest. Ophthalmol. Vis. Sci. **18**(8), 878–881 (1979).
74. Y. Geng, K. P. Greenberg, R. Wolfe, D. C. Gray, J. J. Hunter, A. Dubra, J. G. Flannery, D. R. Williams, and J. Porter, "In vivo imaging of microscopic structures in the rat retina," Invest. Ophthalmol. Vis. Sci. **50**(12), 5872–5879 (2009).
75. H. Radhakrishnan and V. J. Srinivasan, "Multiparametric optical coherence tomography imaging of the inner retinal hemodynamic response to visual stimulation," J. Biomed. Opt. **18**(8), 086010 (2013).
76. H. Yoshimoto, M. Murata, K. Yamagami, and S. Matsuyama, "Studies on the angioarchitecture of the posterior choroid in rat and role of posterior ciliary vein," Invest. Ophthalmol. Vis. Sci. **19**(10), 1245–1250 (1980).
77. K. Sugiyama, Z.-B. Gu, C. Kawase, T. Yamamoto, and Y. Kitazawa, "Optic Nerve and Peripapillary Choroidal Microvasculature of the Rat Eye," Invest. Ophthalmol. Vis. Sci. **40**(13), 3084–3090 (1999).
78. C. Leahy and V. J. Srinivasan, "Three-Dimensional Optical Coherence Microscopy and Mapping of Angio-Architure in the Central Nervous System," in *The Textbook of Advanced Neurophotonics and Brain Mapping*, Y. Chen and B. Kateb, eds. (CRC Press, Taylor and Francis Group, 2017).
79. C. Leahy, H. Radhakrishnan, G. Weiner, J. L. Goldberg, and V. J. Srinivasan, "Mapping the 3D Connectivity of the Rat Inner Retinal Vascular Network Using OCT Angiography," Invest. Ophthalmol. Vis. Sci. **56**(10), 5785–5793 (2015).

1. Introduction

Optical coherence tomography angiography (OCTA) has enabled depth-resolved imaging of retinal and choroidal vasculature without exogenous contrast [1–8]. However, seemingly artefactual, yet highly repeatable, patterns in OCT angiograms remain challenging to explain. In the retina, an hourglass-shaped signal pattern is prominent in the lumens of large vessels [9–12], while in the choroid, below an intact retinal pigment epithelium (RPE), vessel lumens appear "dark". In all vessels, a relative signal increase, also known as a "projection artifact" or "tail," is visible underneath [13–15].

Current explanations for OCTA image artifacts in the literature are based either on *in vitro* experiments [9] or clinical correlations [15, 16]. The shear-induced orientation of RBCs within the vessel lumen and their orientation-dependent backscattering [9] creates an

hourglass pattern in OCT images of controlled *in vitro* flow, but there is no direct evidence for this effect *in vivo*. The dark appearance of choroidal vessel lumens may be caused by fringe washout in spectral / Fourier domain OCT [9, 17], resulting from the choroid's high perfusion rate and RBC speed [18]. However, contrary to this suggestion, dark choroidal vessels are evident even in OCT angiograms obtained by swept source OCT, which is less susceptible to fringe washout [19]. Alternatively, the dark appearance of choroidal vessel lumens may arise from the optical properties of intervening tissue. While melanin protects the posterior retina and choroid against light-induced toxicity [20], light-tissue interactions in the RPE and posterior layers remain unclear [21–23]. Incident light is most likely scattered and absorbed in the RPE and by choroidal melanosomes, which contain highly absorbing, high refractive index melanin pigment. Multiple scattering by melanosomes in the RPE has been reported to depolarize returning light [24–26]. Also, clinical OCT images of geographic RPE atrophy show higher signal in choroidal lumens [16, 21, 27, 28], and exhibit a clear hourglass pattern [28] depending on the severity of RPE damage. This suggests that the RPE may "mask" vessels underneath, but the degree to which absorption versus scattering contribute to this masking is uncertain. Moreover, RPE atrophy is often accompanied by choriocapillaris atrophy, which may also impact OCTA signals from the choroid and complicate interpretation of clinical OCTA. Hence, one cannot isolate the role of the RPE in OCTA based on clinical images of geographic atrophy.

The tails or projection artifacts beneath large vessels in OCTA are anecdotally attributed to multiple scattering in the optics literature [13]. As these artifacts are a problem in clinical imaging of choroidal neovascularization, recent research has been directed towards post-processing algorithms to remove projection artifacts [13, 14]. Projection artifacts can also be mitigated by tighter focusing achieved by adaptive optics [29, 30], or by using a high NA objective [31] in microscopy. While the multiple scattering theory is plausible based on high RBC forward scattering [32], there is no direct evidence that establishes a causal link *in vivo*. Finally, comparisons of OCTA with histology have shown differences in density localized to specific vascular beds [33]. However, possible systematic errors in OCTA caused by vessel orientation have not been investigated to date. Thus, rigorous and controlled *in vivo* experimental demonstration of the biophysical origins of OCTA artifacts is clearly needed.

Here, we provide direct *in vivo* experimental evidence for the roles of RBC forward scattering, RBC orientation, and melanosomes in the appearances of OCT and OCTA images. To achieve this goal, we performed controlled retinal imaging experiments in pigmented and unpigmented rats, using Intralipid as a dynamic scattering contrast agent. The low anisotropy and high symmetry of Intralipid particles relative to RBCs enabled us to clarify the role of RBC anisotropy and asymmetry in OCT angiography. As investigations were performed at a wavelength (1300 nm) where the melanin absorption (μ_a) is ~18% of melanin absorption at 800 nm [34], scattering effects were favored. This study provides direct *in vivo* experimental evidence for the origins of OCTA image artifacts related to light scattering, which will help to inform the clinical interpretation of OCTA images.

2. Methods

2.1 Intralipid and RBC scattering properties

To achieve the goals of this study, Intralipid-20%, an FDA-approved fat emulsion dietary supplement, was injected as an intravenous bolus, and signal enhancement was quantified at various locations in the OCT angiogram. Several groups have already demonstrated that Intralipid can be used as a contrast agent for OCT angiography [11, 35, 36]. Instead, the goal of this study was to use Intralipid as a "probe," with scattering properties that are different from those of blood, to perturb OCTA images. To visualize these differences, a Gegenbauer-Kernel phase function ($\alpha = 0.49$) for blood [32] and a Henyey-Greenstein phase function [37–39] for Intralipid are shown (Fig. 1(A)), employing approximate anisotropy (g) values for each at 1300 nm. Intralipid particles are spherically symmetric, with diameters ranging from

20 nm to 700 nm with an average of 214 nm [40], and are fairly isotropically scattering (g = 0.35 at 1300 nm) [40]. RBCs, by comparison, are asymmetrically shaped (biconcave disk without applied stress), with a long axis of 6.5 microns and a short axis of 1.5 microns in rats [41–46], and with a long axis of 7.5 microns and a short axis of 2 microns in humans (again, without applied stress) [43, 46–51]. RBCs are highly anisotropically scattering (g ~0.95 at 1300 nm for porcine blood [52] and g = 0.96-0.98 for human whole blood [53]).

The phase functions in Fig. 1(A) show the probability of scattering per unit solid angle for blood (red) and Intralipid (green) as a function of elevation angle. Since blood has a higher scattering coefficient than Intralipid at the concentrations used in this study, blood is more likely to forward scatter than Intralipid, which scatters more isotropically in all directions. Moreover, RBC backscattering is direction-dependent, and RBCs orient themselves in shear flow [9] (Fig. 1(B), 1(D)), whereas Intralipid backscattering is independent of orientation due to spherical symmetry of its constituent particles (Fig. 1(C), 1(E)). Because of these key differences between the contrast agent and blood, by comparing pre- and post-contrast images, we were able to address the role of RBC morphology and scattering properties in OCT angiography.
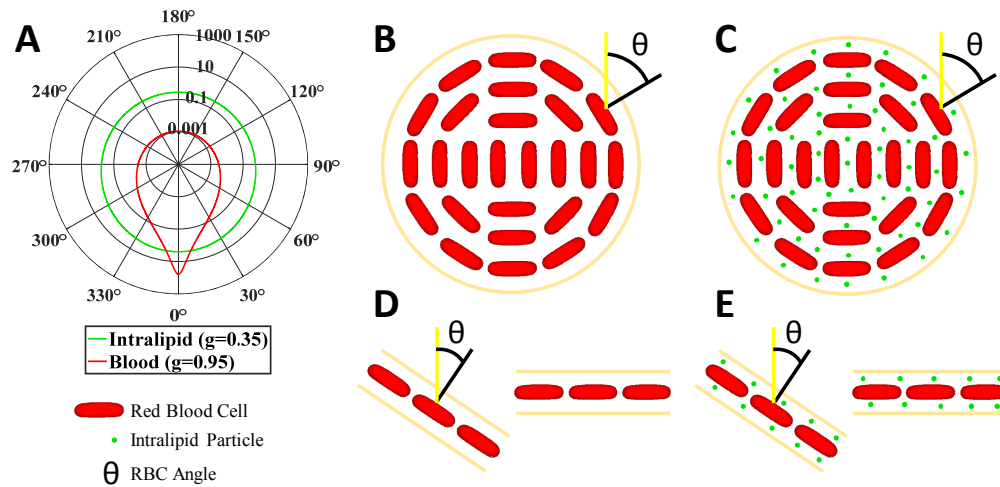

Fig. 1. Optical properties, size, and shape of Intralipid particles are distinct from those of RBCs. A) Blood (RBC suspension) scattering phase function (red, Gegenbauer-Kernel, g = 0.95, α = 0.49) versus Intralipid scattering phase function (green, Henyey-Greenstein, g = 0.35), showing that blood has a significantly higher anisotropy. Forward scattering corresponds to 0° and backscattering corresponds to 180°. Note that phase functions are based on approximate anisotropy (g) values at 1300 nm [40, 52]. (B) Asymmetric RBCs orient themselves due to shear flow in the vessel lumen, with their flat faces pointing outwards, where θ is the angle incident light makes with the RBC normal vector. (C) By comparison, Intralipid particles are smaller than RBCs and more spherically symmetric, with no orientation *per se*. (D) Similarly, in diving or ascending vessels, RBCs are more likely oriented away from the incident light than RBCs in perpendicular capillaries (i.e. capillaries in the *en face* plane). Note, that although RBCs in capillary high shear flow may deform [54–56] from their typical biconcave disk shape, they still retain the orientation shown. (E) By comparison, Intralipid particles lack an intrinsic orientation.

2.2 System design and specifications

A custom periscope sample arm and a reference arm were added to the handheld probe of a commercial Thorlabs TELESTO-II 1300 nm OCT system (Fig. 2), transforming it into a wide-field ophthalmoscope for rat retinal imaging. The probe included a free-space interferometer, fiber coupled to the source and spectrometer. The achievable angular field-of-view (AFOV) of the resulting ophthalmoscope was 53°, about twice that of our previous design [11]. Our results (Fig. 4, Fig. 6, Fig. 7, Fig. 8) represent, to the best of our knowledge,

the largest AFOV rat retinal angiograms and among the highest AFOV cross-sectional rat retinal OCT images reported to date [57–68]. The ophthalmoscope used the rat lens and cornea to focus light on the retina. The rat's ~6 mm axial eye length (measured upon sacrifice and enucleation) and wavelength of 1300 nm [69] resulted in minimal ocular media dispersion. Thus, no dispersion matching with a reference water cell was needed, and residual dispersion could be compensated digitally.

Though high-resolution OCT imaging of the rat retina is possible at 1300 nm [70], absorption in the ocular media is not negligible ($\mu_a = 1.3$ cm^{-1} at 1300 nm for water [71, 72]) and increases for longer wavelengths in the source spectrum. This resulted in a slight loss of axial resolution in the rat retina relative to the nominal axial resolution of 5.2 µm in tissue, determined from the source spectrum.

To convert the TELESTO-II probe into an ophthalmoscope, the scan lens and reference arm were first removed from the probe chassis. The new ophthalmoscope sample and reference arms were built on cage systems, and connected to the TELESTO-II chassis via custom adaptors. The TELESTO-II source employs two superluminescent diodes (SLDs) combined via a fiber coupler, isolated by a circulator, and delivered to the probe by an optical fiber. Within the probe, an output power of 3 mW from the optical fiber was collimated and split evenly by a 50/50 beam splitter into the reference and sample paths (Fig. 2(B)). In the new sample arm, an achromatic doublet pair ($f_{eff} = 100$ mm) was positioned so that the galvanometers fell near the back focal plane of the pair to achieve quasi-telecentricity. The sample arm was transformed into a periscope using a gold-coated elliptical mirror on a right-angle kinematic mount, which reflected the beam to a translatable ocular lens. The ocular lens, consisting of an achromatic doublet pair ($f_{eff} = 25$ mm), was placed 125 mm away from the scan lens so that they combined to form a Keplerian telescope with a magnification of 0.25. The resulting measured beam diameter was 1.1 mm ($1/e^2$), chosen to be significantly less than the dilated rat pupil (3 mm) [73, 74] to avoid aberrations, and possible vignetting at the edge of the field-of-view.

A custom-made aluminum adaptor connected the reference arm to the TELESTO-II chassis. The reference arm contained the same lenses as the sample arm. All lenses were stacked inside a lens tube, and translated together with a mirror on an adjustable mount (Fig. 2(A)). The back-reflected light from the sample and reference arm were combined and re-coupled to the system's optical fiber, sent through a circulator, and finally, to the system's spectrometer (Fig. 2(C)).

The maximum sensitivity of the system, measured by attenuating the reflection from a mirror at a 91 kHz A-scan line rate, was ~92 dB. Raw data for repeated B-scans were acquired using the commercial software, and later post-processed in MATLAB to generate OCT intensity and angiogram images.
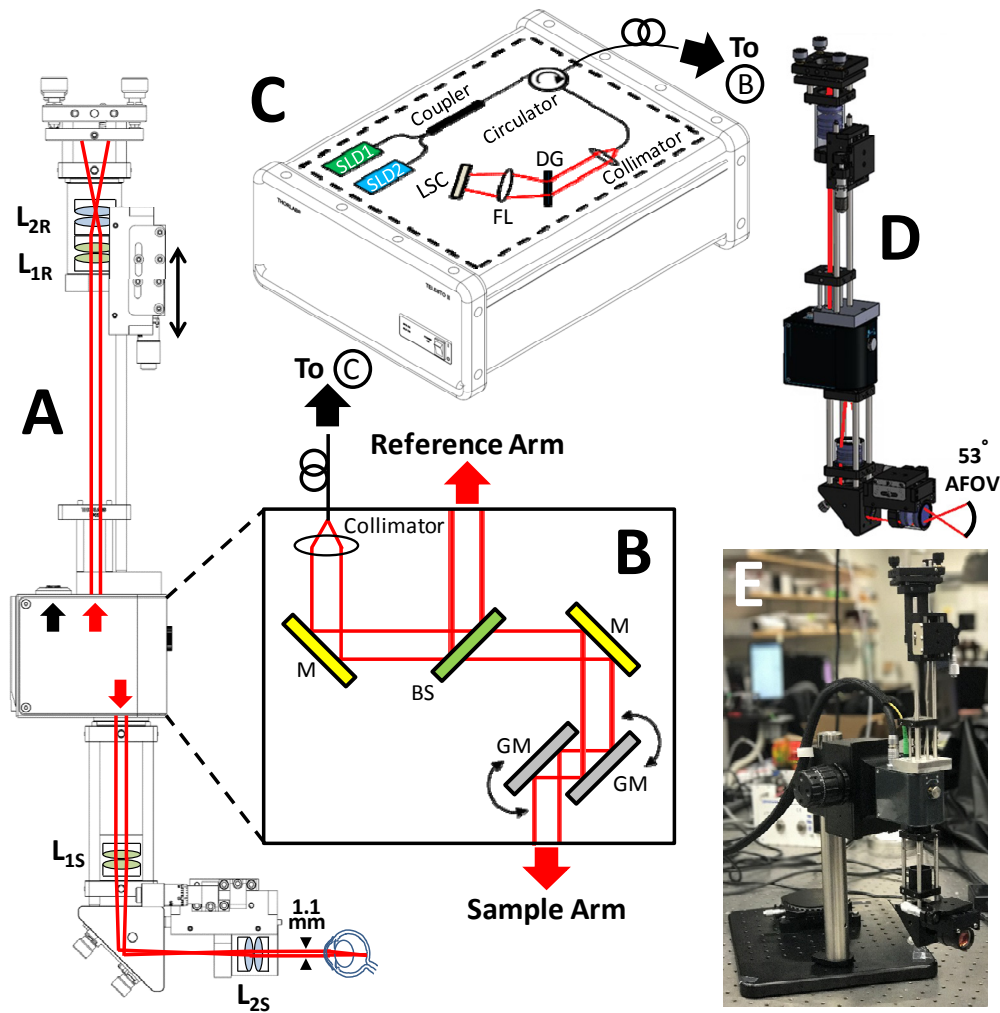
Fig. 2. (A) Schematic of ophthalmoscope based on modifying a Thorlabs TELESTO-II OCT system. In the sample arm, optics were added to demagnify the beam to 1.1 mm, and in the reference arm, dispersion-matched optics were added on a translation stage (double sided arrow) with a mirror. (B) Schematic of optical components inside TELESTO-II chassis. (C) Thorlabs source and spectrometer that fiber couples to TELESTO-II chassis (B). (D) Optical ray trace through a 3D rendering of the ophthalmoscope, showing a 53° angular field-of-view. (E) Photo of ophthalmoscope. L_1: f_{eff} = 100 mm achromatic doublet pair, L_2: f_{eff} = 25 mm achromatic doublet pair, S: sample arm, R: reference arm, GM: galvanometer mirror, BS: beam splitter, LSC: line-scan camera, DG: diffraction grating, SLD: superluminescent diode, FL: focusing lens. Solid black lines indicate optical fibers, while red lines indicate free-space infrared paths.

2.3 Animal preparation

Sprague-Dawley (n = 4, unpigmented) and Long Evans (n = 3, pigmented) rats weighing 250-400 g were anesthetized with 1-2% isoflurane via a custom anesthesia mask, and ventilated using 80% medical air and 20% oxygen. The animals were secured for imaging in a custom-made stereotactic frame, while a heating blanket was used to maintain a core temperature of 37° C.

A peribulbar or retrobulbar injection was administered using 0.1 mL of 2% lidocaine to provide anesthesia and avoid eye rolling. The pupil was dilated using tropicamide. A zero-power contact lens was applied to the eye with Goniovisc, an index matching medium, to

prevent dehydration of the cornea during imaging. All experimental procedures and protocols were approved by the UC Davis Institutional Animal Care and Use Committee.

2.4 Volumetric OCT angiography

Before and after DyC-OCT injection, volumes were acquired to generate three-dimensional angiograms. Volumes consisted of 1500 axial scans at 1500 y-locations with 3 repeats per y-location over a 2.9 mm x 2.9 mm x 1.9 mm range (in tissue). OCT volume angiography was implemented using complex subtraction of consecutive frames after phase correction [75]. In order to preserve information about the magnitude of dynamic scattering, normalization and thresholding were not applied. Angiographic data sets were averaged to 1500 x 1500 x 512 voxels. The scan angle of the galvanometer, the magnification of the Keplerian telescope, the estimated eye length, and Snell's law, where the refractive index of air and tissue are 1 and 1.33, respectively, were used to calculate the transverse retinal FOV. The image volume size was limited mainly by PC RAM.

2.5 2D Wide-field dynamic contrast OCT (DyC-OCT)

During DyC-OCT injection, a sequence of B-scans was acquired at a single y-location over time to generate angiographic movies showing the contrast dynamics. The movies consisted of 500-1000 B-scans or frames. Each B-scan consisted of 1000-2428 axial scans over a 2.0-4.1 mm transverse range. Axial and lateral sample motion were determined by cross-correlation, and then corrected by frame shifting prior to analysis. As above, angiograms were computed via complex subtraction of consecutive frames after phase correction. Changes in the angiogram signal due to tracer injection were quantitatively determined. The signal change during bolus passage is affected by flow, which determines how rapidly the tracer enters and leaves the local circulation. The steady state signal change, after tracer recirculation, is more directly related to blood concentration, and is thus of greater interest for the aims of this study.

The total bolus volume was 3 mL/kg weight, injected via the tail vein. An assumed rat blood volume to body mass ratio of 6.4 mL/100 g thus corresponds to an Intralipid-20% to blood volume fraction of 0.047 mL/mL (4.7% volume fraction).

2.6 Quantification of Intralipid enhancement

To quantitatively assess changes during and after Intralipid injection, an enhancement factor was defined as the ratio of the signal change (tracer signal) to the baseline angiogram signal:

$$\text{enhancement factor} = \frac{\text{tracer angiogram signal}}{\text{baseline angiogram signal}} \qquad (1)$$

Equation (1) compares the regional tracer signal either during bolus passage or at steady state (i.e., after recirculation) to the regional baseline signal. Regions selected for enhancement factor calculation (Fig. 3(A)) included retinal and choroidal vessel lumens (red and green, respectively), retinal and choroidal vessel projection tails (yellow and orange, respectively), and non-projection (non-tail) regions in the inner retina and sclera (blue and purple, respectively). Both superficial (vitreal) and plexiform layer retinal vessels of >25 μm diameter (i.e. no capillaries) were included in the enhancement factor analysis. Vessel sizes are summarized in Fig. 3(B)-3(C).
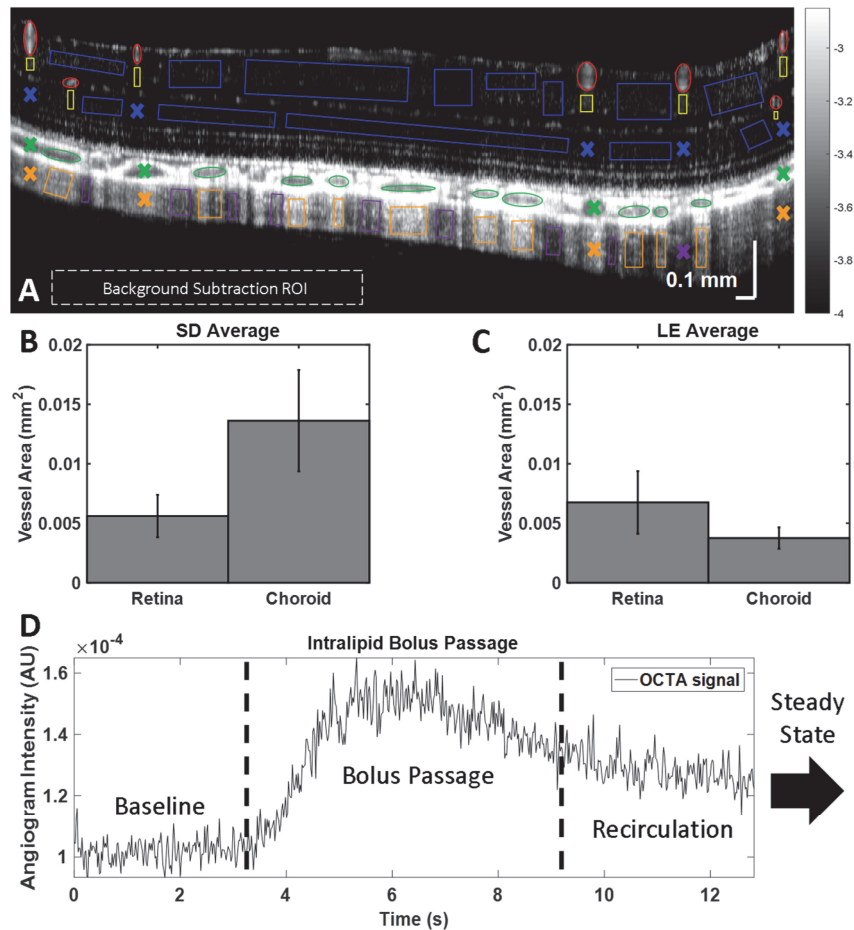
Fig. 3. (A) Angiogram of the posterior pole of a pigmented rat, showing ROIs chosen for analysis: retinal and choroidal vessel lumens (red and green), retinal and choroidal vascular projections (yellow and orange), and "non-tails" in the inner retina and sclera (blue and purple). (B-C) Areas of retinal and choroidal lumens selected for enhancement factor calculations in unpigmented (SD) and pigmented (LE) animals. (D) An example mean signal time course, with baseline, bolus passage, and recirculation before a steady state is reached. Error bars indicate standard errors.

Angiogram signal time courses were examined in manually selected ROIs. An example of the mean signal time course in a vessel lumen during tracer passage is shown in Fig. 3(D). The time course consists of the rising edge, bolus passage, and decay to a steady state plateau after homogenization of the concentration in the bloodstream. Baseline, bolus passage, and steady state time windows were designated for each vessel lumen (Fig. 3(D)). A range of ~250–1250 frames (depending on the frame rate and chosen time window) were averaged to determine regional signals at baseline, during bolus passage, and at steady state. For each vessel, the time windows were selected manually based on the lumen time course, and the same time windows were used for each vessel lumen and its corresponding tail. For inner retinal and scleral non-tail regions (which possess no corresponding lumen) the baseline time window was taken from the beginning of acquisition to the first rising edge across all retinal lumens and choroidal lumens, respectively. For inner retinal and scleral non-tail regions, the steady state time window was taken from the last decay and plateau across all retinal and choroidal lumens, respectively, until the end of the acquisition. For inner retinal and scleral non-tail regions, the bolus passage time window was taken from the first rising edge to the

last decay and plateau across all retinal and choroidal lumens, respectively. The mean signals over the appropriate time windows were always used in determining enhancement factors.

Table 1. ROI number for enhancement factor measurements (Fig. 3)

	SD					LE			
	1	2	3	4	Total	1	2	3	Total
Retinal Vessel	4	2	8	4	18	3	7	9	19
Retinal Tail	4	2	8	4	18	3	7	9	19
Retinal Non-Tail	13	8	10	12	43	9	14	11	34
Choroidal Vessel	5	5	4	4	18	7	14	10	31
Choroidal Tail	5	5	4	4	18	7	14	10	31
Choroidal Non-Tail	5	6	3	6	20	18	10	11	39

The number of ROIs selected in Long Evans and Sprague-Dawley rats for enhancement factor calculations are documented in Table 1. Row colors correspond to ROI colors in Fig. 3(A).

All enhancement factors were calculated after subtracting the mean background signal level, to avoid biasing results. Vessels, tails, or non-tail regions located under a large retinal vessel were excluded from ROI selection, as indicated by the color-coded X's. When selecting non-tail regions, microvasculature in the plexiform layers was also deliberately avoided to prevent confounds from microvascular enhancement.

3. Results

First, we describe qualitative differences in baseline OCTA images of pigmented and unpigmented rats. Next, we demonstrate Intralipid enhancement in retinal, choroidal, and choriocapillaris OCTA images. Finally, we quantitatively analyze Intralipid enhancement during bolus passage and steady state (after tracer recirculation). To enable quantitative analysis, normalization to mitigate static tissue artifacts was not applied.

3.1 Pigmentation and projection artifacts in the sclera

Wide-field OCT angiograms (Fig. 4) show important differences in the vascular projections or "tails" between pigmented and unpigmented rats. First, we observe that the tails are always more prominent in angiograms than in the intensity images. Second, we observe that for the pigmented rat, the tails are clearly defined as bright streaks in the angiograms, whereas in the unpigmented rat, they are less prominent, but still discernible.
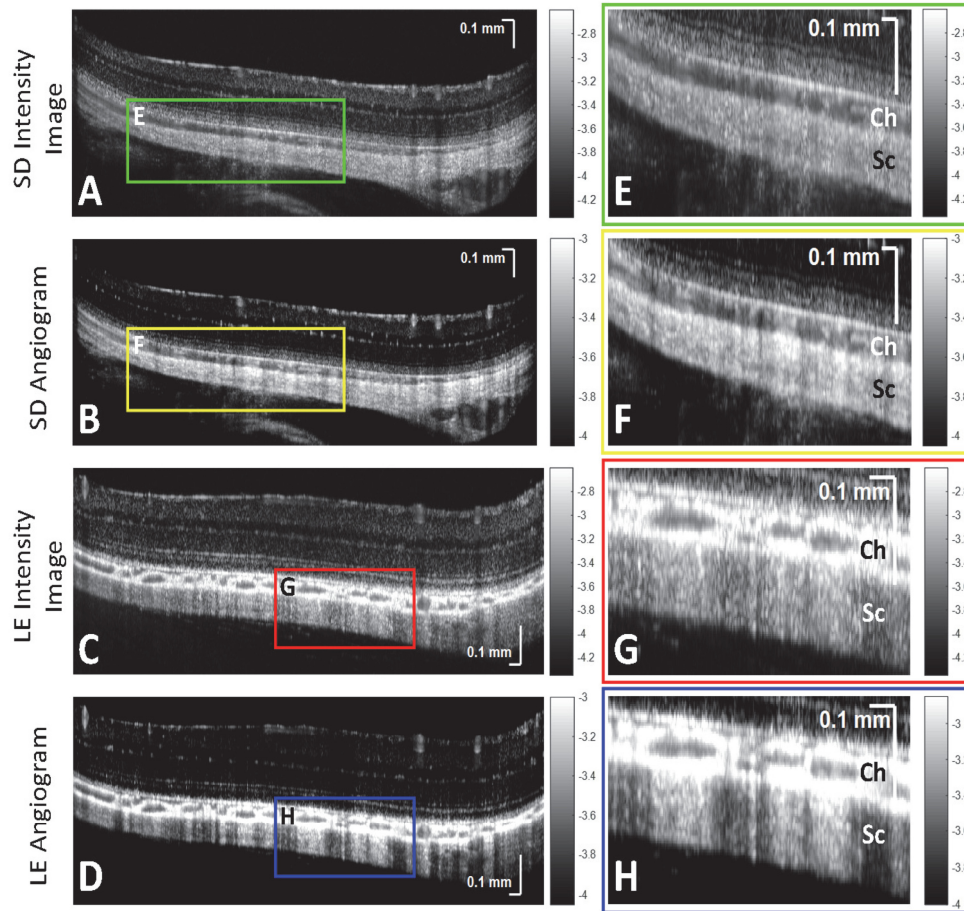
Fig. 4. Pigmentation affects the appearance of "projection" artifacts of choroidal vessels. Sprague-Dawley (SD) and Long Evans (LE) OCT intensity and angiogram images (first column), along with zooms of choroid (Ch) and sclera (Sc) (second column), are shown. (A,B,E,F) Projections of choroidal vessels in a Sprague-Dawley rat are visible but not prominent in scleral regions. (C,D,G,H) Projections of choroidal vessels in a Long Evans rat are much more prominent in scleral regions. Projections are always more prominent in angiograms (B,F,D,H) than intensity images (A,C,E,G). Images are on a logarithmic scale (color bars in log units).

3.2 Cross-sectional OCTA enhancement

Next, contrast enhancement was examined in OCTA cross-sections. Baseline OCTA signal is mainly due to RBCs (Fig. 5(A)), while the change relative to baseline, averaged over the bolus passage (Fig. 5(B)), can be attributed to the tracer. The overlay of the two (baseline-red, tracer-green) across the posterior pole visualizes trends in enhancement (Fig. 5(C)). The vessels in Fig. 5(D), either long posterior ciliary arteries and/or veins and adjacent branching vessels [76, 77], exhibit a clear hourglass artifact. From a zoom of the inner retina (Fig. 5(E)), retinal vessel sides appear green, while the tops appear red and yellow, due to RBC orientation within the lumen (Fig. 1(B)-1(C)). At the same time, vertical capillaries appear green, while horizontal capillaries appear more red and yellow, due to capillary orientation (Fig. 1(D)-1(E)). Additionally, the retinal vessel tails are purely red, suggesting that the tracer negligibly contributes to increasing the projection artifact.
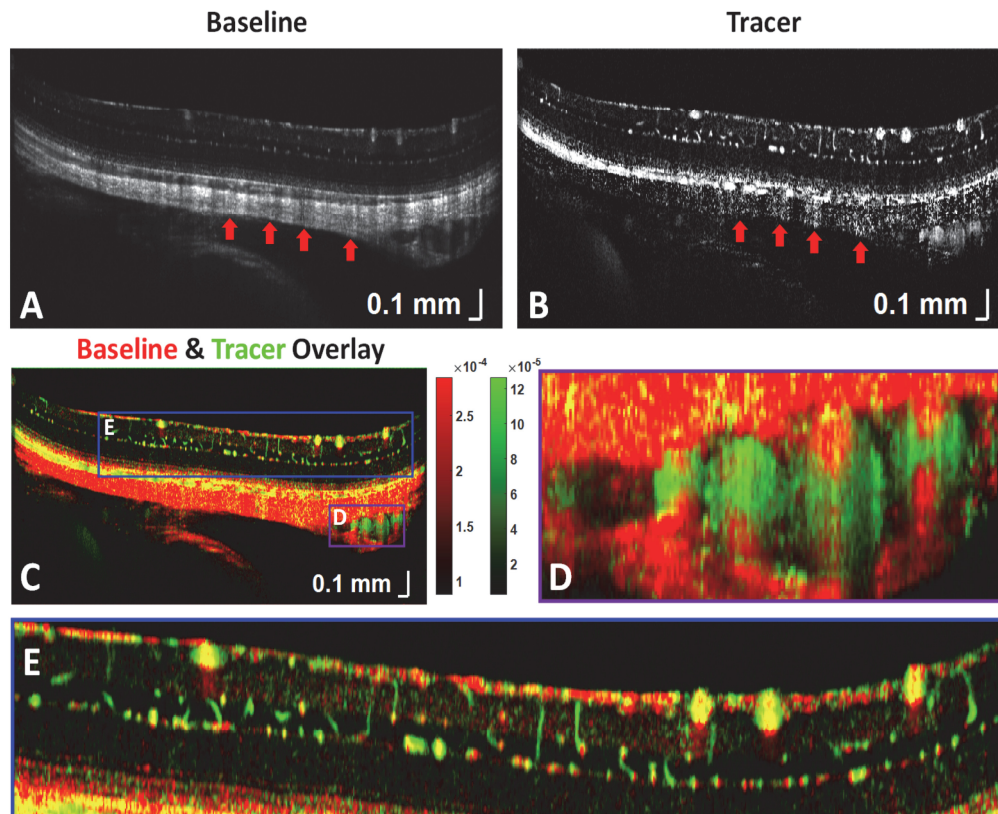
Fig. 5. (A) Baseline OCT angiogram, showing RBC backscattering in the posterior pole of an unpigmented Sprague-Dawley rat. (B) Tracer signal during bolus passage. (C) Color overlay of (A) and (B), where red represents RBC signal, green represents tracer signal, and yellow includes both. Regions with large enhancement factors [Eq. (1)] are green, while regions with small enhancement factors are red. (D) The long posterior ciliary vessels seen within the sclera also demonstrate a prominent hourglass pattern. (E) Zoom of the inner retinal vasculature shows that vertical capillaries and retinal vessel sides are greener (tracer signal weighted), horizontal capillaries and retinal vessel tops are more yellow and red, and retinal vessel tails are purely red (RBC signal weighted).

3.3 Volumetric OCTA of the rat retina, choroid, and choriocapillaris

Next contrast enhancement was examined in OCTA volumes. *En face* OCTA images of the retina and choroid before and after contrast injection are shown in Fig. 6 (first and middle column, respectively). In both pigmented and unpigmented animals, pre-contrast OCT retinal angiograms, based on RBC scattering, clearly show the large arteries and veins emanating from and returning to the optic disk, respectively. However, microvasculature is not as clearly defined. Post-contrast OCT angiograms show increased and more homogenous signal in retinal microvasculature (middle column). Signal from choroidal vasculature generally increased as well, though not as markedly. In the last column of Fig. 6, an algorithm employing a Hessian-based Frangi filter in 3 dimensions was applied to enhance the angiogram signal from tubular structures, and further improved visualization of vasculature, as previously described [78]. For the retina and choroid, a Frangi filter with a scale range (in microns) of 3-21 and 9-21, respectively, and a step size (in microns) of 3 was used. Frangi filter enhanced images should be interpreted with care as false-positive vessels may occur if the scale size of the filter is near the speckle size.
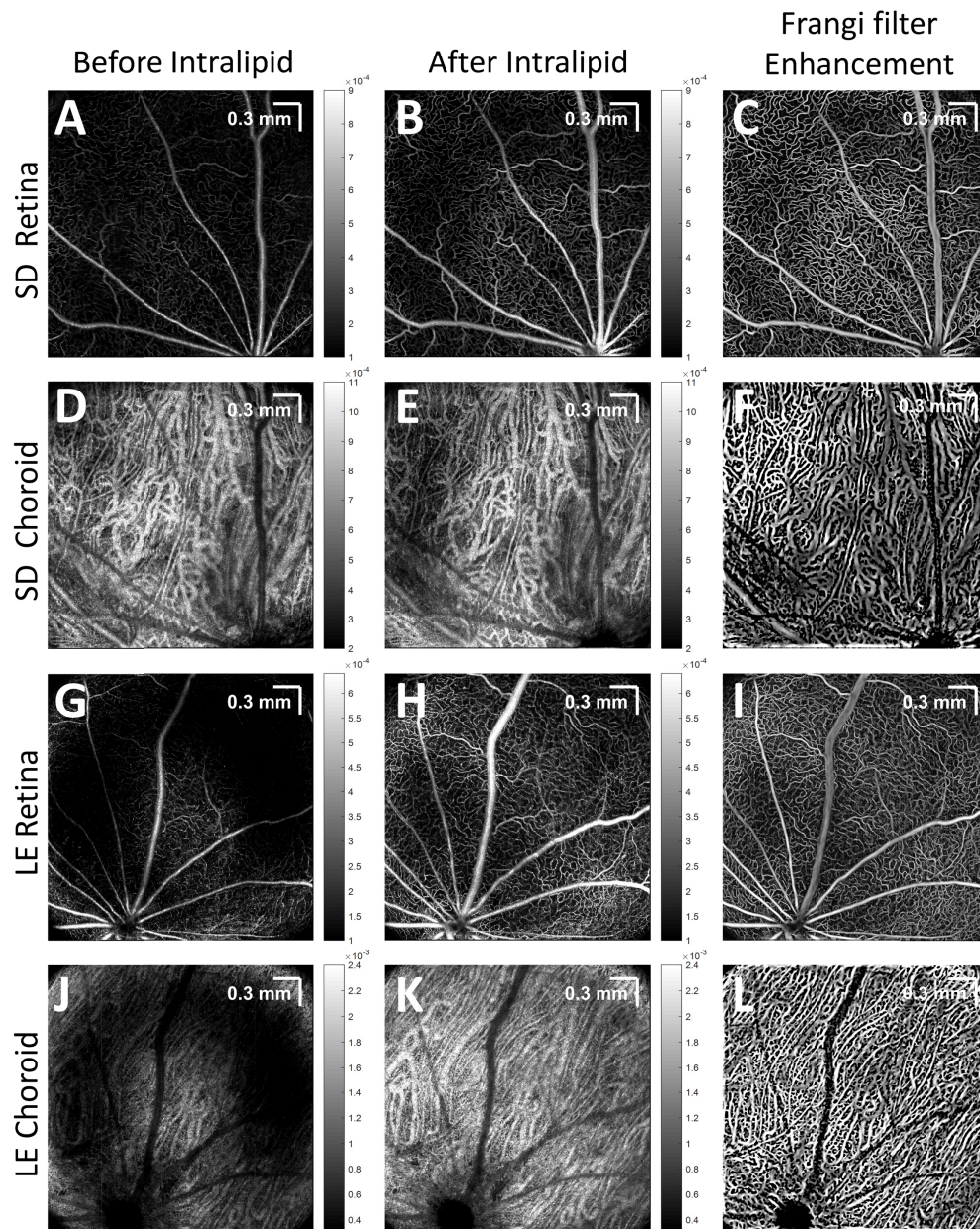
Fig. 6. Enhanced visualization of vascular networks in the retina and choroid was achieved by Intralipid contrast injection, and further improved by the Frangi filter. (A,D,G,J) Pre-contrast, (B,E,H,K) post-contrast, and Frangi filter enhanced (C,F,I,L) retinal and choroidal angiograms of unpigmented Sprague-Dawley (SD) and pigmented Long Evans (LE) rats are shown. Images are on a linear scale (color bars in linear units).

In some animals, the choriocapillaris, a fine microvascular bed beneath Bruch's membrane, was better visualized after contrast administration. A color *en face* image of vasculature underlying Bruch's membrane in an unpigmented rat is shown (Fig. 7(A)). The color scale is based on distance posterior to Bruch's membrane, with green being closer to Bruch's membrane, and red being further away. The choriocapillaris was digitally sectioned in depth and shown as a grayscale image (Fig. 7(B), 7(C)). A Hessian-based Frangi filter was

applied in three-dimensions to highlight the highly anastomosed microvasculature (Fig. 7(D)-7(F)). For the choriocapillaris, a Frangi filter with a scale range (in microns) of 7.5-12 and a step size (in microns) of 1.5 was used.
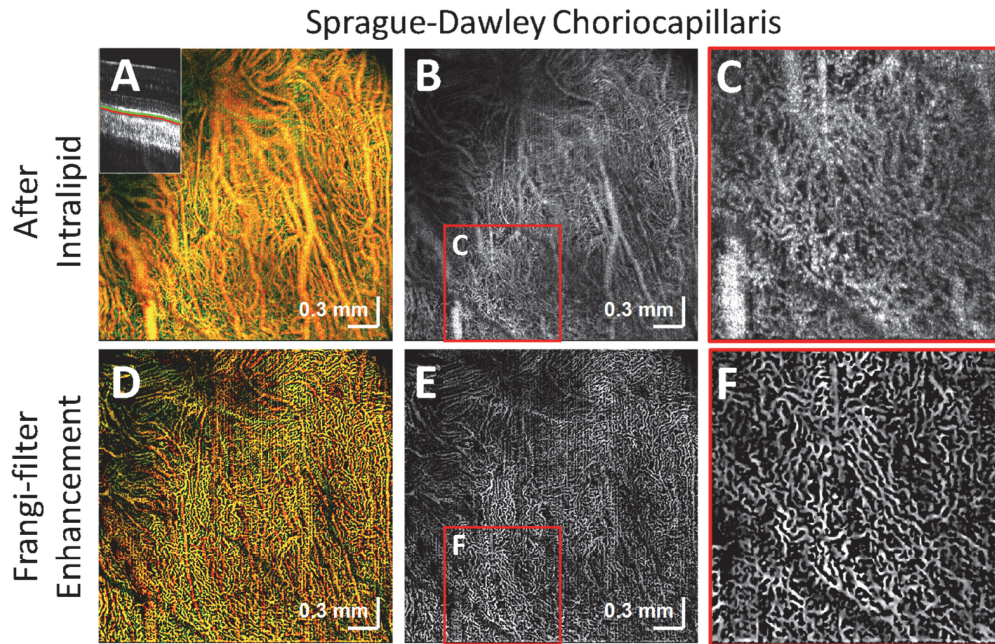

Fig. 7. Visualization of the dense microvascular networks of the choriocapillaris of an unpigmented rat was achieved with Intralipid contrast. (A) Color-coded *en face* image of vasculature underlying the RPE (inset: depth ranges for green and red channels). (B-C) Image formed by selecting depths corresponding to the choriocapillaris. (D,E,F) A three-dimensional Hessian-based Frangi filter was applied to aid in visualizing the delicate and intricate choriocapillaris network.

3.4 Tracer reduces the hourglass artifact

OCT angiograms were visualized qualitatively at three different time points: before bolus passage (baseline), during bolus passage (bolus passage), and after bolus passage (steady state) (Fig. 8). Baseline (red), bolus passage (blue), and steady state (green) images of large retinal and choroidal vessels show the initial presence of an hourglass pattern within the lumen, which disappears after Intralipid injection. This observation further motivates the quantitative analysis described in the next section.
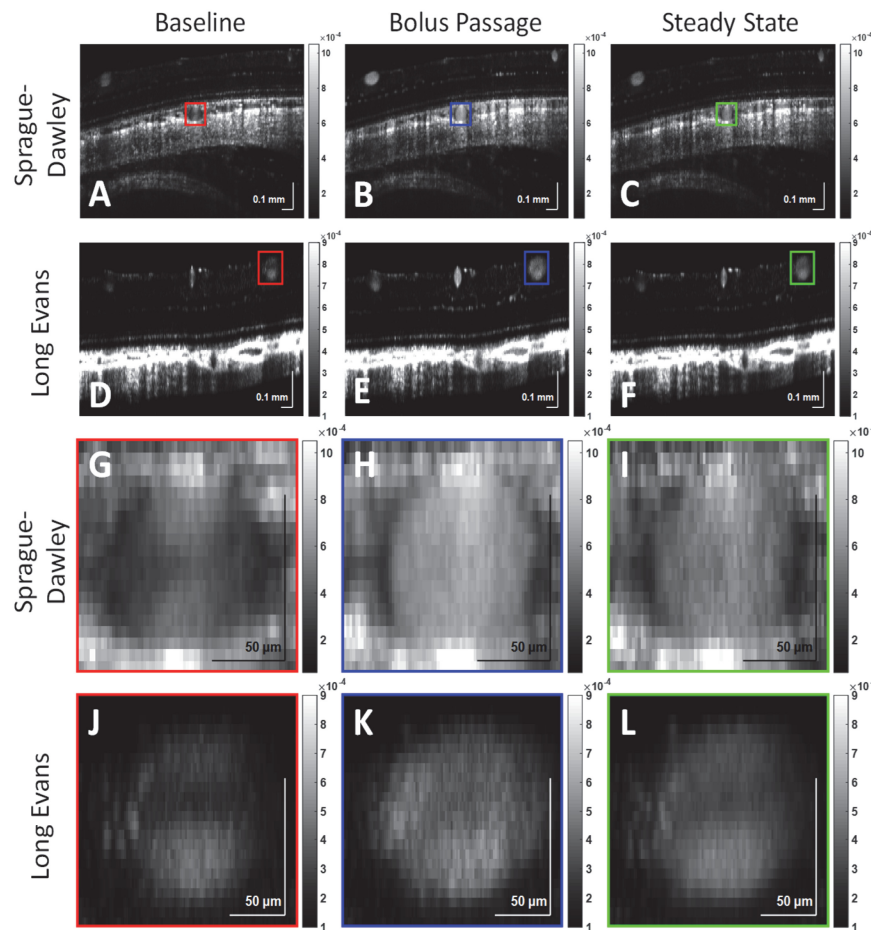
Fig. 8. Angiograms of the posterior pole in a Sprague-Dawley and a Long Evans rat at baseline (A,D,G,J), during bolus passage (B,E,H,K), and at steady state (C,F,I,L) are shown. At baseline, a Sprague-Dawley choroidal vessel lumen (G,H,I) and a Long Evans retinal vessel lumen (J,K,L) show an hourglass shape, which disappears after the introduction of Intralipid tracer into vasculature. Images are on a linear scale.

3.5 Quantitative analysis of tracer enhancement

With an Intralipid injection of <5% blood volume, retinal vessel lumens enhanced by >50% at steady state on average (Fig. 9). Choroidal vessels consistently enhanced less than retinal vessels, particularly at steady state (seen visually in Fig. 6), and tails of choroidal vessels showed a slight negative enhancement, corresponding to a signal decrease, in both strains. Additionally, a tail and non-tail enhancement factor comparison was conducted (Fig. 10). Tails and non-tails of choroidal vessels generally demonstrated consistent and statistically significant increases or decreases within an individual rat, but did not show a consistent trend across rats.

Vessel areas (mm^2) were also measured manually for all analyzed vessels (Fig. 3(B), 3(C)). On average, larger choroidal vessel areas were measured in unpigmented animals than in pigmented animals. Choroidal vessels were also noticeably larger in Sprague-Dawley *en face* angiograms (Fig. 6). Retinal and choroidal lumen enhancement factors at bolus passage and steady state were plotted against vessel area (not shown). Although the data showed a weak trend of lower enhancement with increasing vessel area up to 0.06 mm^2, the correlation was not strong enough to conclude that lumen enhancement depends on vessel area.
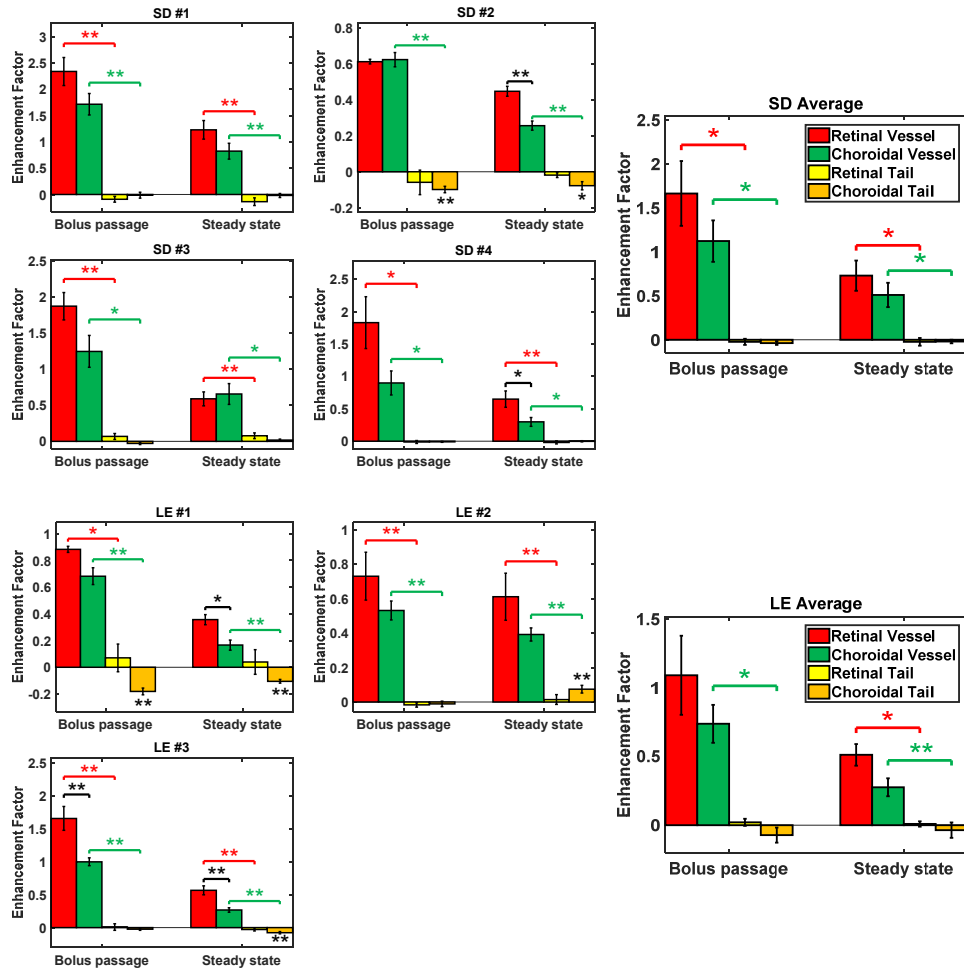
Fig. 9. Enhancement factors [Eq. (1)] for retinal and choroidal vessels and tails in individual Sprague-Dawley (SD, n = 4) and Long Evans (LE, n = 3) rats, and averages for each strain. Similar trends in retinal and choroidal vessel enhancement factors were observed in all rats. Since experimental data were approximately Gaussian (not shown), parametric statistical tests were used. Colored horizontal brackets indicate statistically significant paired t-tests between vessels and tails for the retina (red) and the choroid (green). Black horizontal brackets indicate statistically significant unpaired t-tests between retinal and choroidal vessels: p < 0.05 (*) and p < 0.01 (**). Error bars indicate standard errors.

Motivated by examples in Fig. 5 and Fig. 8, we proceeded to quantify localized changes in the hourglass pattern within vessel lumens. In Fig. 11(A), the sides of the vessel lumen (red dashed outlines) and the top of the lumen (white dashed outline) are shown. The fractional change of the sides-to-top ratio was then computed:

$$\text{fractional change} = \frac{\text{enhanced sides-to-top ratio}}{\text{baseline sides-to-top ratio}} - 1$$
$$= \frac{\text{sides enhancement factor} + 1}{\text{top enhancement factor} + 1} - 1 \tag{2}$$

The "bottom" of the lumen was excluded from this measurement due to attenuation of light passing through the lumen. For this analysis (Fig. 11(B)-11(C)), the large vitreal vessels of the superficial retina were pooled across all rats of the same strain. Small vessels, typically

found in the plexiform layers, were excluded from this measurement due to the difficultly in accurately selecting sides and top regions for these lumens. Choroidal vessels were pooled similarly across rats of the same strain. In both unpigmented and pigmented rats, the lumen sides enhanced more than the lumen top in both the retina and choroid (Fig. 11(B)-11(C)). In pigmented rats, fractional changes in the sides-to-top ratio was lower in choroidal than retinal vessels (Fig. 11(C)).
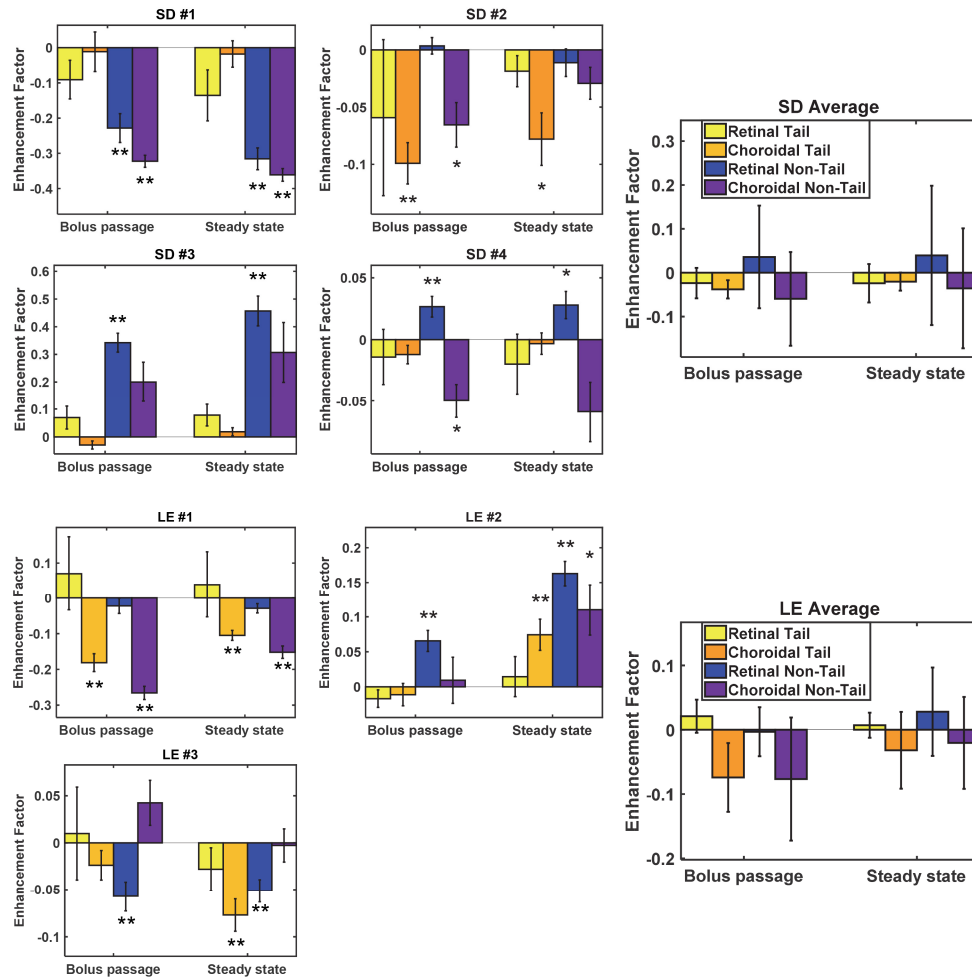

Fig. 10. Enhancement factors [Eq. (1)] for retinal and choroidal tails and non-tails in individual Sprague-Dawley (SD, n = 4) and Long Evans (LE, n = 3) rats, and averages for each strain. No consistent trends in retinal and choroidal tail and non-tail enhancement factors were observed across rats. Asterisks indicate statistically significant t-tests for each measurement group: p < 0.05 (*) and p < 0.01 (**). Error bars indicate standard errors.
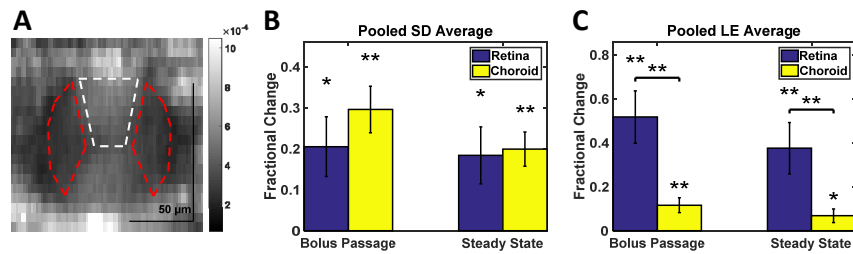
Fig. 11. Quantification of relative signal enhancement in different regions of the hourglass pattern. (A) Red dashed ROIs indicate the sides of the vessel lumen, while the white dashed ROI indicates the top of the lumen. Both red dashed ROIs provide a single sides signal for each vessel. (B,C) The fractional change [Eq. (2)] of the sides-to-top signal ratio is shown for each vessel type (retina and choroid), with vessels pooled across all rats of the same strain: Sprague-Dawley (SD) or Long Evans (LE). Among retinal vessels, only superficial (vitreal) vessels were included in this analysis. Horizontal brackets indicate statistically significant unpaired t-tests between retinal and choroidal lumens, while asterisks directly above bars indicate t-tests for individual groups: $p < 0.05$ (*) and $p < 0.01$ (**). Error bars indicate standard errors.

4. Discussion

In this study, using a 1300 nm wide-field ophthalmoscope, OCT and OCTA imaging of the posterior pole with >50° AFOV was performed in pigmented and unpigmented rats (Fig. 4, Fig. 6, Fig. 7, Fig. 8). Our analysis of enhancement due to Intralipid injection provides causal evidence for the origins of artifacts in OCT angiography, as detailed below.

4.1 RBC orientation impacts backscattered signal in OCTA

An hourglass pattern is commonly observed in large retinal vessels in OCT and OCTA [9–12]. This pattern has been attributed to the aligning of RBCs in shear flow and their orientation-dependent backscattering, both of which are consequences of particle asymmetry [9, 12]. Intralipid particles are spherically symmetric, unlike RBCs, and do not possess an orientation *per se*.

After Intralipid injection, we observed the hourglass pattern diminish in retinal and choroidal vessels (Fig. 8) [11]. Our follow-up quantitative analysis consistently showed greater enhancement at the sides than the top of the lumen, for both retinal and choroidal vessels (Fig. 11). This data provides direct, *in vivo* evidence supporting the hypothesis that the hourglass artifact arises from RBC asymmetry and orientation in shear flow. Moreover, depending on the image gray level, the hourglass pattern is not always visually apparent in images of choroidal vessels (Fig. 4(G)-4(H)). Yet, here we show that even in choroidal vessels, the sides enhance more than the tops after Intralipid injection, suggesting that RBC orientation effects are present and quantifiable in the choroid (Fig. 11(B)-11(C)), even if they are not always observed in images. Finally, we note that the interconnectivity of choroidal vessels may lead to more complex intravascular scattering patterns, such as the "figure-of-88" pattern observed in confluent retinal veins, which was described previously [12].

Our data also reveal that RBC orientation also impacts the visibility of capillaries in OCTA. The overlay in Fig. 5(E) shows that diving or ascending vessels (i.e., those connecting the ganglion cell layer / nerve fiber layer, inner plexiform layer, and outer plexiform layer), enhance much more than perpendicular capillaries in the *en face* plane that reside in a single layer. While we cannot rule out possible differences in hematocrit, the most plausible explanation for the differing enhancement factors is that RBCs in diving or ascending vessels present a lower backscattering cross-section to the incident light than RBCs in capillaries that lie in the *en face* plane (Fig. 1(D)-1(E)). Graphing results obtained previously using OCTA without a contrast agent need to be interpreted based on this new finding [79].

4.2 Projection artifacts are due to multiple scattering

Projection artifacts or tails are high signal regions extending to path lengths longer than the vessel lumen, i.e. appearing "beneath" vessel lumens in OCTA (Fig. 4 and Fig. 5(C), 5(E)). The multiple scattering hypothesis suggests that these artifacts correspond to light paths comprising both RBC small-angle forward scattering events and tissue backscattering events. High RBC anisotropy (Fig. 1(A)) would make such paths particularly likely within large vessels. In this study, when Intralipid, with a comparatively low anisotropy (Fig. 1(A)), was injected into the blood stream, the signal from the vessel lumen increased, while the signal "beneath" the vessel lumen in the tail region did not change appreciably (Fig. 9). This difference in enhancement is explained by the higher ratio of forward to backscattering probability for RBCs compared to Intralipid particles (Fig. 1(A)). The fact that a low anisotropy tracer markedly enhances the intraluminal signal, without significantly perturbing the tail artifacts, suggests that forward scattering is necessary to cause projection artifacts. Thus, our data support the multiple scattering hypothesis for tail artifacts.

4.3 The impact of melanosomes on OCTA images

Our direct comparison of pigmented and unpigmented rats shows that melanosomes provide a highly bright backscattering "background," against which choroidal lumen signal appears dark (Fig. 4). Moreover, melanosomes in regions between choroidal vessels attenuate light, making the multiple scattering tails appear comparatively more prominent in the sclera, particularly in angiograms of pigmented eyes (Fig. 4(H)).

In spite of the very different appearances of vessels in baseline OCT images and angiograms, the enhancements of Sprague-Dawley and Long Evans choroidal vessels were more similar. The overall lower vessel enhancement factors in Long Evans compared to Sprague-Dawley rats (Fig. 9) may be due to different tracer-to-blood volume ratios. For choroidal vessels, the sides enhanced more than the tops, regardless of pigmentation (Fig. 11). This suggests that the shear-induced orientation persists in the choroid, although the hourglass pattern may be less visually apparent in images.

Finally, the choroidal vessel sides-to-top fractional change was, firstly, lower in pigmented than in unpigmented rats (Fig. 11(B)-11(C)), and secondly, lower in choroidal vessels than in retinal vessels of pigmented rats (Fig. 11(C)). Both findings suggest that multiple scattering of melanosomes may make the hourglass pattern less prominent. This is consistent with clinical geographic atrophy images [28] where loss of melanosomes reveals the hourglass artifact in choroidal vessels. Multiple scattering from the intact, pigmented RPE and choroid could broaden the angular distribution of light, thus making the hourglass pattern, which requires a well-defined angle between light paths and RBCs (Fig. 1(B)), less evident. Finally, the possibility that hemodynamics, and in particular, shear forces, differ between rat strains cannot be excluded as an explanation for the less prominent hourglass pattern in Long Evans choroidal vessels.

4.4 Unexplained observations in the choroid

Several observations in the choroid do not have a clear explanation. The first unexplained observation is that choroidal vessel lumens enhance less than retinal vessel lumens, in both pigmented and unpigmented rats (Fig. 6 and Fig. 9). Though this observation would be explained if choroidal vessels had a higher hematocrit (fractional RBC volume) than retinal vessels, we were unable to find any supporting evidence in the literature. Another possible explanation is optical: if the light returning from the choroid is multiply scattered, then the multiply scattered choroidal vessel signal would be less sensitive to introduction of Intralipid than singly backscattered signal from retinal vessels. However, this second explanation would require the RPE and intervening tissue to multiply scatter light in both pigmented and unpigmented rats, since both strains showed lower choroidal vessel lumen enhancement. This

multiple scattering explanation is more likely to apply to pigmented rats, which contain highly scattering melanosomes, than unpigmented rats, where lipids are probably responsible for scattering of the RPE. Finally, different shear rates in the choroid could lead to differing degrees of RBC elongation [9], which may also affect enhancement factors.

The second unexplained observation is that, though tails and non-tails of choroidal vessels generally exhibited consistent and statistically significant increases or decreases within an animal, there were no consistent trends across rats (Fig. 10). In general, Intralipid injection was expected to increase intravascular scattering and thereby reduce the signal from the sclera, including choroidal tail (scleral regions underneath large choroidal vessels) and non-tail (scleral regions without a large overlying vessel) regions. This behavior was observed in some, but not all, animals. Interestingly, choroidal tails were not reduced more than non-tails by the Intralipid injection, even though the intravascular path length is much longer. This observation may be explained by the multiple scattering in large vessels, which results in attenuation that is less than predicted by single scattering theory. Surprisingly, for some rats, signal from the sclera increased after the injection (see Fig. 5(B) and Fig. 10). Other eyes showed increases in choroidal and retinal vessel tail and non-tail signal, suggesting the presence of motion. Explanations for these inconsistencies could be attributed to variations in choriocapillaris and choroidal thickness, and compression of the sclera due to the injection. Finally, it is important to state that enhancement factors in extraluminal tail and non-tail regions were always much smaller in magnitude than enhancement factors in vessel lumens (Fig. 9). Thus, the unexplained observations in this section do not affect the main conclusions of the study.

4.5 Study limitations

In this study, controlled and stabilized imaging in the rat retina allowed us to compare enhancements quantitatively between retinal and choroidal vessels, with and without pigmentation. The slight differences in shape between human and rat RBCs, as well as different vessel sizes, hemodynamics, ocular morphology, and melanosome content, may prevent the results of this study from being applied directly in humans. The OCT wavelength in this study (1300 nm) is also longer than the OCT wavelengths used in clinical ophthalmology (800 nm or 1050 nm). Nevertheless, the general conclusions regarding the biophysics of light interactions accounting for OCTA image appearance should be applicable to humans.

5. Conclusion

In this work, we provided direct evidence for the roles of red blood cell (RBC) rheology, morphology, and scattering properties in creating OCTA artifacts. We achieved this by employing an intravascular contrast agent with a distinct size, shape and scattering anisotropy. We assessed the impact of RBC orientation on intravascular scattering patterns and vessel detectability, the role of RBC forward scattering in projection artifacts, and the influence of melanosomes on the OCTA signal from the choroid and sclera. This work provides the first controlled *in vivo* experimental data to help explain OCTA image appearance, and will advance the interpretation of clinical OCTA images.

Disclosures

Vivek J. Srinivasan receives royalties from Optovue, Inc.